1. The New Tolerance Factor

The perovskite crystal structure is defined by the chemical formula ABX_3. Here A and B can span the periodic table, and the anion X is typically a chalcogen or halogen. To visualize the structure, it contains a network of corner-sharing BX_6 octahedra surrounding a larger A-site cation. Generally, in the said structure, the ionic radius of A site, r_A is much larger than ionic radius of B-site, r_B. Ideally, perovskites have cubic crystal lattice, but distortions from the cubic structure can arise from size mismatch of the cations and anion, resulting in additional perovskite structures or non-perovskite structures. So, while designing any perovskite for a specific application, assessment of the stability of its structure is primordial. A new tolerance factor (NTF) by C J Bartel et al.[1], proves to be a descriptor-based approaches enabling a high-throughput screening for the stability. It is defined as $\tau = \frac{r_X}{r_B} - n_A\left(n_A - \frac{r_A/r_B}{ln\left(r_A/r_B\right)}\right)$, here r_A, r_B and r_X are ionic radii of A-site, B-site and an anion respectively, and n_A is oxidation state of A-site (weighted average if more than one cations exist at A-site). For a stable perovskite structure, A and B must be chosen in such a way that $r_A \gg r_B$. Otherwise as $r_A/r_B \to 1$, and the probability of formation, $P(\tau)\to 0$. Further the octahedral factor $\frac{1}{\mu} = r_X/r_B$ sets a condition on the choice of r_B for a given anion X. If $r_B \ll r_X$, then τ improves beyond the accepted limit and leads to $P(\tau)\to 0$. These conditions thus state that for a stable perovskite ground state, τ must be less than 4.18, and μ should be greater than 0.414. Before the application of NTF one must carefully consider all possible oxidation state of A and B cations that charge balance X_3. If more than one charge-balanced pair exists, a single pair is chosen based on the electronegativity

ratio $\frac{\chi_M}{\chi_N}$ of the two cations. If 0.9 < $\frac{\chi_M}{\chi_N}$ < 1.1, the pair that minimizes $|^{n_M} - {}^{n_N}|$ is chosen, otherwise, the pair that maximizes $|^{n_M} - {}^{n_N}|$ is chosen. Note that the suffixes M and N denote any random A and B if the compound is new. To know the possible oxidation states for each cation, Shannon's ionic radius database is used[2,3]. In the present case for $BaTiO_3$ the charge-balance pair is straight forward, which is $[Ba^{2+},Ti^{4+}]O^{6-}_3$. For $La_{0.835}Na_{0.165}MnO_3$, there are two cations at the A site of which La has a single oxidation state, 3+. The charge-balance pair is thus $[La^{3+},Mn^{3+}]O^{6-}_3$. However, Na is in 1+ oxidation state and as there are large possible oxidation states of Mn ranging from 2+ to 7+, the situation becomes slightly tacky. A simple calculation shows that in case of a system where La^{3+} is substituted by Na^{+} the average oxidation state that Mn can have to charge balances O^{6-}_3 is 3.33. So, the possible oxidation state for the Mn is 4+ and charge-balance pair is $[Na^{3+},Mn^{4+}h]O^{6-}_3$ where h is hole. Based on these assignments, the ionic radii of A and B-site cations are chosen close to 12 and 6 coordinates respectively. But in manganites the coordination number can go as low as 8 for highly distorted structures. The ionic radii of Ba^{2+} and Ti^{4+} in 12 and 6 coordination respectively are 1.61Å and 0.605Å. Similarly, the ionic radii of La^{3+}, Na^{+}, Mn^{3+} and Mn^{4+} are respectively 1.36Å, 1.39Å, 0.645Å and 0.53Å. The ionic radius of O^{2-} is 1.40Å. The NTF thus estimated for $BaTiO_3$ is 3.75 and for $La_{0.835}Na_{0.165}MnO_3$ it is 2.59. The μ is 0.46 and 0.43 respectively for $BaTiO_3$ and $La_{0.835}Na_{0.165}MnO_3$. The values of τ and μ are well within the constraints of stable perovskite structure. If the composites are considered, they are expected to hold immiscible perovskite structure same as that of the parent compounds.

2. The profile matching using Le Bail method

These days any diffraction data can be handled using whole powder pattern fitting which includes whole powder pattern decomposition (WPPD, also called as profile matching) and Reitveld analysis (also called as structure matching)[4]. The latter uses Wyckoff position of the atoms, their isotropic Debye-Waller factors, and the occupancies to calculate the intensities and to generate the powder pattern to compare with the obtained one. In contrast WPPD doesn't require any prior knowledge of atomic attributes. The WPPD includes two methods viz. The Pawley method and the Le Bail method (LB). The Le Bail method is most often used WPPD method which begins with arbitrary values of intensities which evolve iteratively upon assigning to estimates of divided data amongst the contributing reflections. In this method, estimates to cell parameters, peak profile parameters, zero shift of the sample and background function can also be obtained along with the with the Le Bail intensity extraction. The advantage of LB is that it is the only way to intensity extraction when structure is unknown or vague. Also, LB is preferential over Rietveld method when experimental artefacts are difficult to model, as may be the case in situ diffraction. The WPPD is becoming increasing popular as its can be a precursor for structure matching. Say when the structural model is very crude, it is advisable to analyse the pattern first with the LB to obtain the cell parameters, profile shape function and, background before running the Rietveld refinement. However, as the constraint used in WPPD are few and simpler compared to Rietveld method, it is more prone to give ambiguous results if profile shape parameters or microstructural parameters are refined[5].

The most useful output of the Le Bail method is that it generates the Miller indices (hkl) corresponding to each phase, which enables comparison with standard sample and hence confirms the structure. In the present investigation the generated (hkl) values of $BaTiO_3$ ($p4mm$ space group) and $La_{0.835}Na_{0.165}MnO_3$ ($R\bar{3}c$ and $I\ 1\ 2/a\ 1$ space group) are given in table 1.

Table 1. tabulation of 2θ versus (hkl) corresponding to the major phase of $BaTiO_3$ and $La_{0.835}na_{0.165}MnO_3$ (tetragonal, rhombohedral and monoclinic respectively).

BL0		BL100			
$P4mm$		$R\bar{3}c$		$I\,1\,2/a\,1$	
2θ (degree)	hkl	2θ (degree)	hkl	2θ (degree)	hkl
22.019	(001)	22.965	(012)	19.748	(110)
22.247	(100)	22.965	(012)	22.869	(200)
31.502	(101)	32.597	(110)	22.904	(011)
31.667	(110)	32.808	(104)	32.428	(-211)
38.906	(111)	38.529	(113)	32.505	(020)
44.908	(002)	40.251	(202)	32.725	(002)
45.394	(200)	40.602	(006)	32.75	(211)
50.669	(102)	46.924	(024)	38.3	(-121)
51.002	(201)	51.262	(211)	38.374	(-112)
51.113	(210)	52.721	(122)	38.374	(310)
55.989	(112)	53.006	(116)	38.44	(121)
56.3	(211)	58.167	(300)	38.653	(112)
65.765	(202)	58.301	(214)	40.031	(-202)
66.143	(220)	58.702	(018)	40.116	(220)
69.907	(003)	62.273	(125)	40.568	(202)
70.365	(212)	68.289	(220)	46.719	(400)
70.639	(221)	68.779	(208)	46.794	(022)
70.73	(300)	71.897	(131)	50.966	(-312)
74.389	(103)	71.957	(223)	51.018	(-321)
75.103	(301)	72.256	(217)	51.106	(130)
75.192	(310)	72.495	(119)	51.352	(321)
78.775	(113)	73.102	(312)	51.633	(312)
79.477	(311)	73.34	(036)	52.428	(-411)
83.529	(222)	73.34	(306)	52.48	(-222)
87.376	(203)	73.816	(110)	52.566	(031)
87.807	(302)	77.854	(134)	52.865	(013)
88.152	(320)	78.203	(128)	52.865	(411)
		81.36	(315)	52.916	(222)
		82.349	(042)	57.798	(-402)
		82.579	(226)	57.943	(-231)
		83.038	(0210)	58.019	(-213)
		86.968	(404)	58.067	(420)
		87.881	(0012)	58.148	(231)
				58.615	(402)
				58.631	(213)
				61.922	(-132)
				61.922	(330)
				61.995	(510)
				62.042	(-123)
				62.119	(132)
				62.336	(123)

				67.898	(-422)
				68.075	(040)
				68.587	(004)
				68.646	(422)
				71.434	(-512)
				71.55	(-332)
				71.569	(-323)
				71.569	(-521)
				71.65	(-141)
				71.742	(141)
				71.983	(-114)
				72.026	(521)
				72.098	(332)
				72.347	(114)
				72.347	(512)
				72.39	(323)
				72.641	(-413)
				72.755	(-431)
				72.855	(240)
				72.99	(-204)
				72.99	(600)
				73.118	(033)
				73.118	(431)
				73.714	(204)
				73.729	(413)
				77.394	(-611)
				77.506	(-233)
				77.604	(042)
				77.927	(611)
				77.969	(024)
				78.039	(233)
				80.844	(-341)
				80.9	(-314)
				81.011	(530)
				81.108	(341)
				81.784	(-602)
				81.953	(314)
				82.005	(-242)
				82.19	(-224)
				82.19	(620)
				82.355	(242)
				82.835	(602)
				82.89	(224)
				86.401	(-404)
				86.62	(440)
				87.791	(404)
				89.64	(-523)
				89.709	(-532)

				89.927	(150)

3. Meaning of Reliability Factors

In principle the difference profile plot (difference curve) is the best way to validate the Le bail fitting and Rietveld refinement, however there are numerical parameter which would authenticate the goodness of fit. They are called as reliability factors or agreement indices or R values. Such R values are the weighted-profile R value (R_{wp}), the statistically expressed R value (R_{exp}), the Bragg-intensity R value (R_B). As the R_{wp} is background sensitive it is always preferential to have this value without the background contribution. Ideally for a best fit the R_{wp} must approach R_{exp} and the R_B must be small but positive value. Also, the ratio of R_{wp} to R_{exp} $(R_{wp}/R_{exp} = \chi^2)$ should approach to unity. However, this value depends on R_{exp}. Suppose the data is over collected, R_{exp} will be very small and consequently the χ^2 will be quite larger than 1 and on the other way for a under collected data, R_{exp} will be very large and hence χ^2will less than 1. So, it is wise to consider the R values and their proximity to each other, than considering the ratio of them. Further R_{wp} obtained for a structure free fitting (Le Bail fitting) is excellent indicator of best fit and should approach the statistically expected R value. Also, the R_{wp} Reitveld refinement must agree with the $R_{wp}$of LB[6].

4. The Origin of Lognormality in Grain Size Distribution

A multitude of physical process such as particle size distribution, molar mass distribution, concentration of rare earths in a mineral, growth of the crystal in chemical reaction, size of ice crystals in frozen medium etc. follow lognormal distribution, or in other words, effects that are multiplicative result in lognormal distribution[7]. Plenty of research works consider the particle size distribution to be lognormal distribution based on model of coagulation of Smoluchowsky.

This model deals with a closed system where initially large number of fine particles meet at random to coagulate[8]. It is an ideal treatment and doesn't map into real situations. The coagulation model assumes the lognormality but doesn't explain its origin. However, few recent works have concluded that the origin of lognormality in particle growth distribution lies in time spent for growth. This is true in any growth process where the fundamental mechanism is diffusion and drift through a finite growth region[9]. Accordingly, the rate at which particle mass, and hence the particle volume V changes due to atomic absorption is proportional to the surface area. Further the particle residence time in the active zone is lognormally distributed when the particle transport occurs by means of diffusion and drift[8]. Sometime the description of grain size distribution using lognormal distribution lacks physical basis and researchers tend to use gamma distribution to discuss the particle size distribution. But if the distribution is narrow both the distributions secure similar results[7,10]. The probability density function of a lognormal distribution is defined as $f(x) = \frac{1}{\sqrt{2\pi}ax} exp\left(-\frac{1}{2}\left(\frac{\ln(x) - b}{a}\right)^2\right)$ where x is data ($0<x<\infty$) whose natural logarithms are normally distributed. B is shape or mean (μ) of lognormal distribution and A^2 (σ^2) is its variance or scale. The expectation value or arithmetic mean of x is given by $e^{b+\frac{1}{2}a^2}$, where e^b is the geometric mean or median of the lognormal destitution (mean of corresponding normal distribution) and e^{a^2} is geometric variance. The mode of x is e^{b-a^2}, the standard deviation is $e^{b+\frac{1}{2}a^2}\sqrt{e^{a^2}-1}$ and variance is $e^{2b+a^2}\left(e^{a^2}-1\right)$.

The parabolic rate law is given by $\chi^2 = 2K_P t + C$, where K_P is the parabolic rate constant, t is the dwelling time for anneal, and C is an integration constant. The parabolic rate constant in

air exhibits an Arrhenius-type of behaviour where it depends exponentially on activation energy and inverse of the annealing temperature.

5. The Diffused reflectance and Kubelka-Munk function

Diffused reflectance is an optical phenomenon generally in the ultraviolet, visible and near to mid-infrared region used to obtain molecular spectroscopic information with minimal sample preparation. The surface reflected electromagnetic (EM) spectrum is collected and analyzed usually as function of frequency (wavenumber in cm^{-1}) or wavelength (in nm). Based on the surface which reflects the EM Wave, Reflection is of two types viz. regular or specular reflection (mirrors) and diffused reflection emanating from the mat or dull surfaces. Unlike specular reflection, the diffused reflection is the result of complex optical activity when light illuminated on the dull surface. There occurs reflection, refraction, diffraction and even absorption of certain frequency of light, if the sample is optically active. This means the sample under diffused reflectance spectroscopy (DRS) simultaneously scatters and absorbs EM radiation. Based on the absorption and scattering phenomena, the DRS spectra of the specimen is manipulated using two-constant theories, the notable one is two-constant Kubelka-Munk theory. The absolute remittance of diffusely reflecting sample is the ratio of intensities of reflected to incident radiation which is given by $R_\infty = \frac{J}{I_0}$, here ∞ stands for the thickness of the sample in an ideal condition where no incident light intensity is transmitted. As practically there is no perfectly diffusively reflecting specimen ($R_\infty = 1$) the remittance is considered to be relative and is given by $R_\infty^{'} = {R_{sample}}/{R_{standard}}$. Relative remittance is dimensionless physical quantity and is obtained in percentage ($R\%$). According to Kubelka-Munk theory remittance of DRS is proportional to absorption coefficient α of transmission spectroscopy as $\alpha(\lambda) = A \times F(R)$ where is A is a constant and $F(R)$ is Kubelka-Munk function. The two-

constant Kubelka-Munk function (KMF) is given by $F(R) = {}^{K}/_{S} = \frac{(1-R)^2}{2R} = \frac{2.303\varepsilon C}{2R}$, here K and S are absorption and scattering coefficient respectively, ε is absorptivity and C is the analyte concentration[11].

6. Spin-Glass feature in some perovskite oxides

The cusp in susceptibility is seen in polycrystalline $LaCoO_3$, $La_{0.5}Nd_{0.5}Co_{0.5}Mn_{0.5}O_3$ and $La_{1-x}Sr_xCoO_3$ by P Tiwari et al[12] and J. Wu et al[13] respectively. The origin of SpG like state is consequence of magnetic frustration happening at low temperature due to various competing interaction. For instance, the parent systems such as $LaCoO_3$ which is nonmagnetic insulator, the magnetic interaction originally dominated by antiferromagnetic (AFM) interactions between Co^{3+} ions. As the doping is increased, the fraction of Co^{4+} ions increases and the system phase separates into ferromagnetically interacting hole-rich clusters in an antiferromagnetically correlated matrix[13]. However, if x grows beyond a critical value the FM interactions dominate, and they are distributed randomly as FM clusters in compounds. At the boundaries of these clusters, there still exists the magnetic frustration phenomenon, caused by the competitive interaction. This is the main reason for the occurrence of CG behaviour[14]. Same is the case with $La_{0.5}Nd_{0.5}Co_{0.5}Mn_{0.5}O_3$, but here substitution has led to FEM in the system due to the unequal magnetic moments of the constituent cations and their orientation with the easy axis. The loosely bound spins give glassy nature. Another noteworthy perovskite is $LaNiO_3$, which is known to be a Pauli paramagnetic metallic oxide. The oxygen vacancies in this system are found to induce FM or AFM leading to SpG like state[15]. Unlike $La_{1-x}Sr_xCoO_3$, $LaCo_{1-x}Ni_xO_3$, $LaCo_xMn_{1-x}O_3$, and Ba and Ti substituted $Pb(Fe_{1/2}Nb_{1/2})O_3$ where the competition between AFM (between the same charge species of element) and FM (between different charge species of same element or two or more dissimilar elements) leads to SpG or cluster glass like state[16–19]. In $LaCo_{1-x}Rh_xO_3$ $LaCo_{1-x}Nb_xO_3$, and $La_{(1-2x)}Sr_{2x}Co_{(1-x)}Nb_xO_3$ the

disorder induced by the random distribution Co-rich and Rh-rich clusters of different sizes. The magnetic dilution where long range interaction seizes due to Nb substitution are said to the be the origin of the spin glass behaviour[20–22]. Although SpG like states is not common to nonstoichiometric $BaTiO_3$, the hexagonal $Ba(Ti_{1-x}Mn_x)O_3$ system has shown existence of SpG-like state with paramagnetic background which was not intrinsic to h- $Ba(Ti_{1-x}Mn_x)O_3$ but attributed to segregated and nucleated magnetic species such as Mn_3O_4 upon Mn incorporation[23] . There are several perovskite compositions such as $SrRuO_3/SrIrO_3$ superlattice, $LaAlO_3/SrTiO_3$ Heterostructures[24,25] display spin glass states. Though not mentioned as spin glass dynamics but similar ZFC-FC nature as that of BL0 is evident in perovskites such as $Na_{0.5}Bi_{0.5}TiO_3/Co_{0.025}O_2$ system and $BaIrO_3$[26,27].

7. The Arrott plots (M^2 versus H/M)

The Arrott plots are frequently used to estimate the saturation magnetization (M_S) and nature phase transition, first order and second order. The Arrott plot is variation square of magnetization plotted against the ratio of applied field to saturation magnetization. Here extrapolation of the linear portion of M^2 versus $\frac{H}{M}$ curve to the M^2 axis at higher $\frac{H}{M}$ values gives M_s[28]. According to Banerjee criterion the phase transition is second order (SOPT) or first order (FOPT) if slope of M^2 versus $\frac{H}{M}$ is positive or negative respectively[29,30].

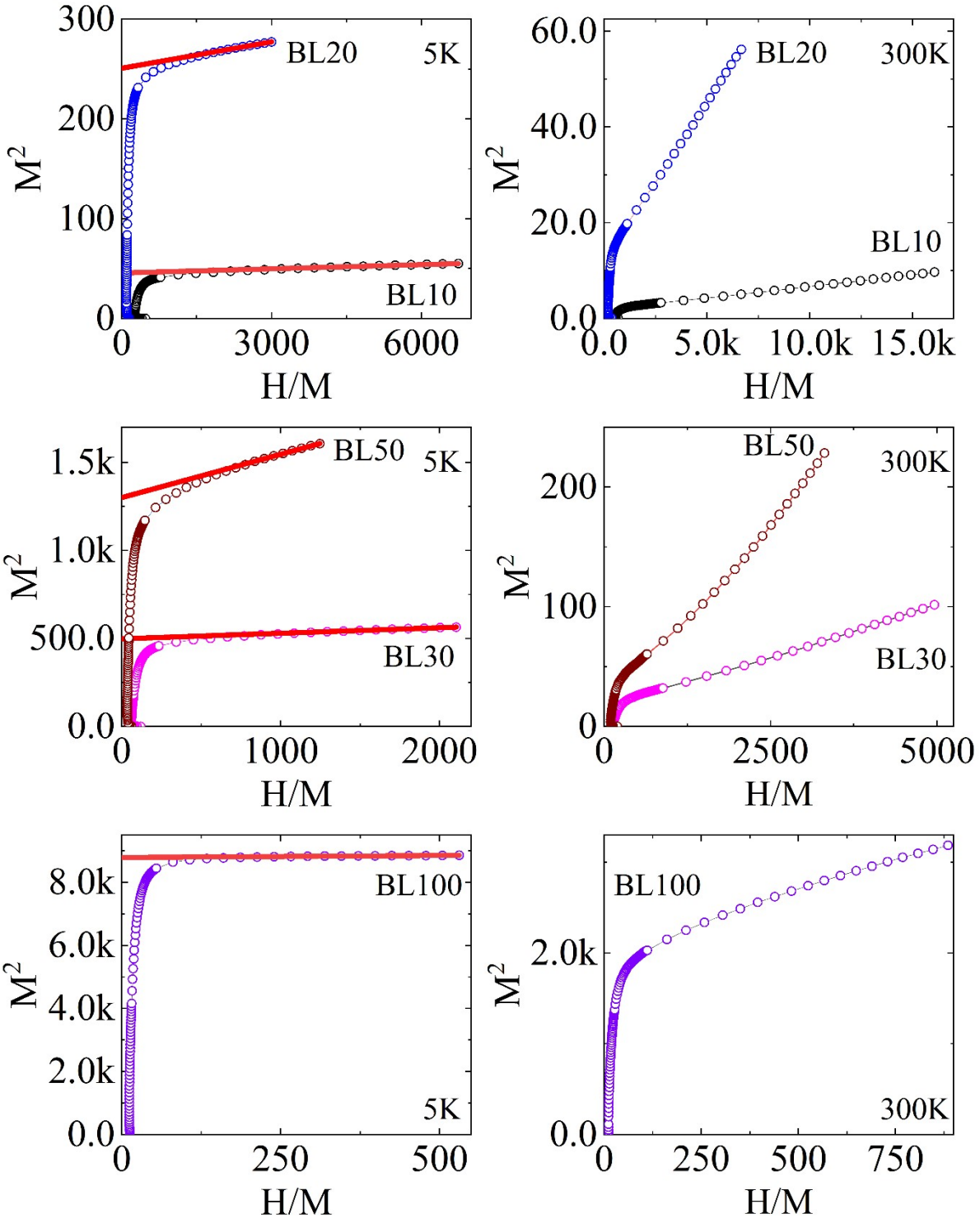

Figure 1. The Arrott plots depicting the variation of M^2 versus $\frac{H}{M}$. The solid line of linear fit to data points (5K) at higher $\frac{H}{M}$ values extrapolated to M^2 axis give the saturation magnetization M_S and positive slope of the curve (300K) indicates SOPT.

References

1 C. J. Bartel, C. Sutton, B. R. Goldsmith, R. Ouyang, C. B. Musgrave, L. M. Ghiringhelli and M. Scheffler, *Sci Adv*, 2019, 5, 1–9.

2 R. D. Shannon, *Acta Crystallographica Section A*, 1976, 32, 751–767.

3 R. D. Shannon and C. T. Prewitt, *Acta Crystallogr B*, 1970, 26, 1046–1048.

4 A. Le Bail, *Powder Diffr*, 2005, 20, 316–326.

5 A. M. Abdulwahab, *Int J Curr Res*, 2013, 5, 2547–2553.

6 L. B. Mccusker, R. B. Von Dreele, D. E. Cox, D. Louër and P. Scardi, *J Appl Crystallogr*, 1999, 32, 36–50.

7 M. Fátima Vaz and M. A. Fortes, *Scripta Metallurgica*, 1988, 22, 35–40.

8 L. B. Kiss, J. Söderlund, G. A. Niklasson and C. G. Granqvist, *Nanotechnology*, 1999, 10, 25–28.

9 J. Söderlund, L. B. Kiss, G. A. Niklasson and C. G. Granqvist, *Phys Rev Lett*, 1998, 80, 2386–2388.

10 G. W. Petty and W. Huang, *J Atmos Sci*, 2011, 68, 1460–1473.

11 F. M. . Mirabella, *Modern techniques in applied molecular spectroscopy*, Wiley, 1998.

12 P. Tiwari, S. A. Atkar, P. Sharma, A. Datta, A. D. Singha, M. Roy-Chowdhury, T. Sarkar and S. Thota, *J Phys D Appl Phys*, 2025, 58, 155301.

13 J. Wu and C. Leighton, *Phys Rev B*, 2003, 67, 174408.

14 T. L. Phan, L. V. Bau, N. V. Khiem, N. X. Phuc and S. C. Yu, *physica status solidi (b)*, 2005, 242, 1522–1527.

15 C. J. Anjeline, B. G. Marate, D. Velu, S. M. S. Kumar and N. Lakshminarasimhan, *Mater Chem Phys*, 2022, 288, 126331.

16 M. Viswanathan and P. S. A. Kumar, *Phys Rev B*, 2009, 80, 012410.

17 C. L. Bull, H. Y. Playford, K. S. Knight, G. B. G. Stenning and M. G. Tucker, *Phys Rev B*, 2016, 94, 014102.

18 Y. Kobayashi, S. Murata, K. Asai, J. M. Tranquada, G. Shirane and K. Kohn, *J Physical Soc Japan*, 1999, 68, 1011–1017.

19 V. V. Laguta, M. D. Glinchuk, M. Maryško, R. O. Kuzian, S. A. Prosandeev, S. I. Raevskaya, V. G. Smotrakov, V. V. Eremkin and I. P. Raevski, *Phys Rev B*, 2013, 87, 064403.

20 H. Guo, K. Manna, H. Luetkens, M. Hoelzel and A. C. Komarek, *Phys Rev B*, 2016, 94, 205128.

21 R. Shukla and R. S. Dhaka, *Phys Rev B*, 2018, 97, 024430.

22 R. Shukla, A. Jain, M. Miryala, M. Murakami, K. Ueno, S. M. Yusuf and R. S. Dhaka, *The Journal of Physical Chemistry C*, 2019, 123, 22457–22469.

23 X.-K. Wei, Y. Su, Y. Sui, Z. Zhou, Y. Yao, C. Jin and R. Yu, *Appl Phys Lett*, DOI:10.1063/1.4811699.

24 B. Pang, L. Zhang, Y. B. Chen, J. Zhou, S. Yao, S. Zhang and Y. Chen, *ACS Appl Mater Interfaces*, 2017, 9, 3201–3207.

25 H. Hu, D. Wang, A. Tseng, Z. Chen, C. Kong, J. Yi and S. Li, *Adv Mater Interfaces*, DOI:10.1002/admi.201800352.

26 A. Kumari, Indian Institute of Technology Hyderabad, 2013.

27 P. Dubbaku Sri, *Evolution of structural, electronic and magnetic properties upon Mg-doping in BaIrO 3*, 2020.

28 R. N. Bhowmik, S. Kazhugasalamoorthy and A. K. Sinha, *J Magn Magn Mater*, 2017, 444, 451–466.

29 J. Mira, J. Rivas, F. Rivadulla, C. Vá Zquez-Vá Zquez and M. A. Ló Pez-Quintela, *Change from first-to second-order magnetic phase transition in La 2/3 (C a, S r) 1/3 MnO 3 perovskites*, 1999.

30 L. D. Mendonca, M. S. Murari and M. D. Daivajna, *Physical Chemistry Chemical Physics*, 2022, 24, 13171–13188.